Available online at www.sciencedirect.com
ScienceDirect
Journal of Solid State Chemistry 181 (2008) 685–692
JOURNAL OF SOLID STATE CHEMISTRY
www.elsevier.com/locate/jssc

Preparation of thin layer materials with macroporous microstructure for SOFC applications

D. Marrero-López[a], J.C. Ruiz-Morales[a], J. Peña-Martínez[a], J. Canales-Vázquez[b], P. Núñez[a,*]

[a]*Department of Inorganic Chemistry, University of La Laguna, 38200 La Laguna, Tenerife, Spain*
[b]*Renewable Energy Research Institute, Albacete Science & Technology Park, 02006 Albacete, Spain*

Received 1 September 2007; received in revised form 24 November 2007; accepted 4 January 2008
Available online 11 January 2008

Abstract

A facile and versatile method using polymethyl methacrylate (PMMA) microspheres as pore formers has been developed to prepare thin layer oxide materials with controlled macroporous microstructure. Several mixed oxides with fluorite and perovskite-type structures, i.e. doped zirconia, ceria, ferrites, manganites, and NiO–YSZ composites have been prepared and characterised by X-ray diffraction (XRD), scanning electron microscopy (SEM), transmission electron microscopy (TEM), nitrogen adsorption and mercury porosimetry. The synthesised materials are nanocrystalline and present a homogeneous pore distribution and relatively high specific surface area, which makes them interesting for SOFC and catalysis applications in the intermediate temperature range.

Keywords: SOFC; Electrolytes; Electrodes; PMMA; Macroporous materials

1. Introduction

One of the major targets for the development of solid oxide fuel cell (SOFCs) is the reduction of the operating temperatures [1–3]. Thus, different strategies have been envisaged as the development of thin film configurations [4], alternative electrolytes with higher conductivity than the stabilised zirconia [5–9] and new electrode materials [10–13]. Another key issue is the electrode microstructure as pore size, morphology and electrode porosity govern the transport of gaseous species through the electrodes, hence affecting the electrode performance [14]. Nowadays, the electrodes are commonly deposited by screen-printing on the electrolyte and the porosity is controlled using pore formers, which are generally organic compounds and/or graphite [1,15]. However, it is difficult to control the pore distribution using this method, giving rise to microstructures with non-uniform geometry and low specific surface areas. A precise control of the porosity and a larger specific surface area of the electrode may improve the cell performance as a consequence of an increase in the concentration of active sites where the electrochemical reactions occur. Ruiz-Morales et al. [16] have recently reported that the performance of a cell with YSZ electrolyte, LSM–YSZ composite as cathode and NiO–YSZ as anode is improved by up to 30% using a combination of nanometric oxide powders and polymer microspheres as pore former to control the porosity of the electrodes. Previously, Zhang et al. [17] found that the electrochemical performance of Ni–YSZ anode was notably improved by optimising the porosity, using a similar procedure. However, this method is only applicable when the starting oxide powders have a particle size distribution in the nanometric range, which is not always possible. Furthermore, the high firing temperatures required to ensure good contact between particles causes a significant decrease in the specific surface area of the starting nanoparticles due to particle agglomeration and sintering.

Porous materials with high relative surface area can also be obtained by using a colloidal crystal templating method [18–20]. In this case, a colloidal crystal template is prepared via a regular arrangement of organic microspheres (e.g. polymethyl methacrylate PMMA). The interstices in the

*Corresponding author. Fax: +34 92 2318461.
E-mail address: pnunez@ull.es (P. Núñez).

0022-4596/$ - see front matter © 2008 Elsevier Inc. All rights reserved.
doi:10.1016/j.jssc.2008.01.008

template are generally filled by infiltration of alkoxide precursors, which are solidified by a sol–gel transition. The template is then removed by calcination, yielding three-dimensionally (3D) ordered macroporous materials. Nevertheless, most of the materials prepared by alkoxide sol–gel are single oxides, such as: SiO_2, TiO_2, Al_2O_3; and only some mixed oxides have been reported using this route [20]. Moreover, the alkoxide sol–gel method is not the best choice to prepare mixed metal oxides due to the difficulty and high cost to obtain alkoxide precursors when they are not commercially available. As a consequence, several alternatives have been proposed. Yan et al. reported the preparation of single oxides (e.g. MgO, Cr_2O_3, NiO, ZnO, etc.), using oxalic acid and metal nitrates to form the corresponding metal acetatates [21]. Later, Sadakane et al. [22] reported the preparation of macroporous materials with composition $La_{1-x}Sr_xFeO_3$ using a similar method from metal nitrates and ethylene glycol.

Nowadays, there are a large number of reports on 3D ordered microstructures with applications in areas such as photocatalysis, electronics, magnetism, etc. [1]. However, there exist few references in the literature dedicated to the preparation of macroporous and/or mesoporous materials for SOFC applications [16,17,23–27].

Here we describe a facile and general new method to prepare thin layer oxides with controlled pore size for SOFC applications. The method uses aqueous stoichiometric cation solutions of metal nitrates, citric acid as complexing agent and PMMA microspheres as pore former. Materials obtained by this method were yttria stabilised zirconia (YSZ)—state-of-the-art in SOFC electrolyte—and other electrolytes with higher conductivity than YSZ in the intermediate temperature range, such as gadolinium doped ceria (CGO) and $La_2Mo_2O_9$ (LMO). Ferrite and manganite cathode materials, e.g. $La_{0.7}Sr_{0.3}FeO_{3-\delta}$ (LSF) and $La_{0.8}Sr_{0.2}MnO_{3-\delta}$ (LSM), the anode materials $La_4Sr_8Ti_{11}Mn_{0.5}Ga_{0.5}O_{38-\delta}$ (LSTMG) and NiO–YSZ composites were also prepared using this approach.

2. Experimental

2.1. Synthesis

PMMA microspheres were synthesised by emulsion polymerisation of methyl methacrylate (MMA) in water. The polymerisation starts with the thermal decomposition of an initiator, i.e. 2,2′-azobis(2-methylpropionamidine), rendering two free radicals, which subsequently add to the double bond of MMA. Consecutive addition of MMA monomers to the free radicals end of the polymer chain will increase the polymer size. A more detailed procedure can be found in Ref. [28].

Starting materials used as reagents were: La_2O_3 (99.99%), Gd_2O_3 (99.9%), Y_2O_3 (99.9%), MoO_3 (99.5%), $Ce(NO_3)_4 \cdot 6H_2O$ (99.99%), $Sr(NO_3)_2$ (99.9%), $Mn(NO_3)_2 \cdot 6H_2O$ (99.99%), $Ga(NO_3)_3 \cdot 9H_2O$ (99.9%), $Fe(NO_3)_3 \cdot 9H_2O$ (98%), $Ni(NO_3)_2 \cdot 6H_2O$ (99%), $ZrO(NO_3)_2$ (99.99%) and titanium isopropoxide (97%) from Aldrich. Rare-earth oxides were pre-calcined at 1000 °C for 2 h in order to achieve complete dehydration and decarbonation. The corresponding metal nitrates, which are generally hygroscopic, were decomposed up to 1000 °C in a TG/DTA (Perkin-Elmer, mod. Pyris Diamond) to determine their accurate cation stoichiometry. Stoichiometric solutions of the corresponding cations were prepared by dissolving metal nitrates in distilled water, lanthanide oxides in diluted nitric acid and molybdenum oxide in diluted ammonia. Titanium isopropoxide was first weighed and dissolved in ethanol and then heated at 60 °C with continuous stirring to evaporate the solvent. Citric acid was added as complexing agent to the resulting stoichiometric cation solution with a ligand/metal molar ratio of $L/M = 0.3$–0.5. The pH was adjusted to 3 by adding nitric acid. The final volume of the solution was 25 ml and the cation concentration was adjusted to obtain approximately 1 g of the oxide. Approximately 3 g PMMA microspheres with an average diameter of 400 nm were introduced in the homogeneous cation solution which was then stirred for about 30 min at room temperature. The resulting mixture was deposited by dropwise addition on quartz substrates and left to dry in air at 25 °C for 3 days to slowly evaporate the water. During water evaporation, the PMMA microspheres are ordered by sedimentation and a solid gel is formed and infiltrated between the microspheres (Fig. 1). The specimens were calcined in air at a heating rate of 1 °C/min to decompose the polymer template and reach crystallisation of the compounds, resulting in thin layer oxides with macroporous structure. The optimum calcination temperature of the compounds was investigated by thermogravimetric analysis as summarised in Table 1.

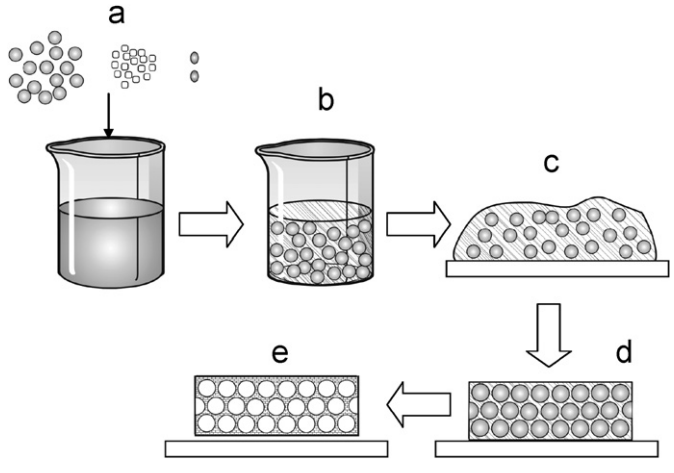

Fig. 1. Schematic diagram of the preparation of thin layer materials with macroporous microstructure. Starting metal salts are dissolved in distilled water, citric acid was used as complexing agent and PMMA microspheres as pore former (a). The homogeneous suspension (b) is deposited on a substrate (c) rendering an ordered template of PMMA microspheres with an infiltrated citrate gel of stoichiometric cations (d). An inorganic porous microstructure is obtained after calcination (e).

Table 1
Composition, structural parameters of the synthesised macroporous materials

Composition	Notation	T_s (°C)	D_{cr} (nm)	s.g.	Cell parameters (Å)	V (Å^3)
$Ce_{0.8}Gd_{0.2}O_{2-\delta}$	CGO	450	9	*Fm*-3*m*	$a = 5.423(5)$	159.35(3)
$Zr_{0.8}Y_{0.2}O_{2-\delta}$	YSZ	650	12	*Fm*-3*m*	$a = 5.1435(4)$	136.08(2)
$La_{0.7}Sr_{0.3}FeO_{3-\delta}$	LSF	650	20	*Pbnm*	$a = 5.512(4)$ $b = 5.551(4)$ $c = 7.795(5)$	238.57(3)
$La_{0.8}Sr_{0.2}$ $MnO_{3-\delta}$	LSM	600	22	*R*-3*c*	$a = 5.482(6)$ $b = 13.32(2)$	357.9(1)
$La_4Sr_8Ti_{11}Mn_{0.5}Ga_{0.5}O_{38-\delta}$	LSTMG	650	22	*Pm*-3*m*	$a = 3.903(3)$	59.47(7)
$La_2Mo_2O_9$	LMO	550	60	$P2_1$	$a = 7.043(2)$ $b = 7.131(9)$ $c = 7.12(1)$ $\beta = 89.68(7)$	346.75(7)
NiO–YSZ	NiO–YSZ	650	$D_{YSZ} = 11$ $D_{Ni} = 18$	*Fm*-3*m*	$a_{YSZ} = 5.114(9)$ $a_{Ni} = 4.177(8)$	$V_{YSZ} = 133.7(4)$ $V_{Ni} = 72.8(2)$

Note: T_s: firing temperature; D_{cr}: crystallite size; s.g.: space group.

2.2. Characterisation

The synthesised materials were characterised by X-ray diffraction (XRD) using a Philips X'Pert Pro diffractometer, equipped with a Ge(111) primary monochromator and a X'Celerator detector. The scans were performed in 2θ range of 5–80° with 0.016° step and acquisition time of 2 h. Structure refinements were performed using FullProf suite [29,30]. The microstructure was examined using a scanning electron microscope (SEM) (JEOL JSM-6300) and by transmission electron microscopy (TEM) (JEOL 2011) operating at 200 kV. The equipments used an Oxford Link detector to perform energy-dispersive X-ray spectroscopy analysis. Samples for TEM observation were prepared by dispersion of a very fine ground powder in acetone and then deposited onto a perforated carbon film supported on a Cu grid.

Nitrogen adsorption isotherms were recorded on a Gemini V (Micromeritics Instrument). The specific surface area was calculated using the multipoint Brunauer–Emmett–Teller (BET) method. Macropore intrusion volumes and macropore size distributions were measured by mercury intrusion porosimetry on an Autopore IV (Micromeritics Instrument) over a pressure range of 0.5–40,000 psi and analysed using the Washburn Equation. Prior to nitrogen sorption and mercury intrusion porosimetry measurements, all the samples were degassed at 200 °C under a constant flow of dry N_2 overnight.

3. Results and discussion

Some requirements are necessary for the preparation of macroporous materials by templating method; for instance, the infiltrated solution must be solidified before the polymer template decomposes. Additionally, a stoichiometric distribution of cations is necessary during the solidification process to avoid phase segregations after crystallisation. Citric acid is a complexing agent that ensures a homogeneous distribution of cations during this process and moreover the gels obtained from citrate solidify at rather low temperatures.

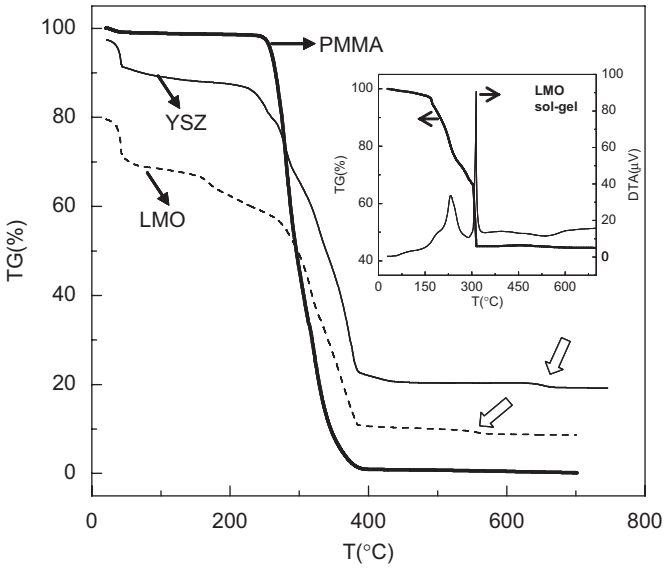

Fig. 2. TG curves of the as-prepared PMMA microspheres and infiltrated specimens of PMMA–YSZ and PMMA–LMO. The curves were shifted for better visualisation. The inset shows TG–DTA curves for LMO gel after dried in air.

A thermogravimetric study of the decomposition processes corresponding to the individual solid gels and infiltrated samples was followed by TGA under air flow at a heating rate of 5 °C/min. The TG curves of PMMA microspheres and some infiltrated samples are illustrated in Fig. 2. The inset of Fig. 2 shows the decomposition curve of a representative dried gel of $La_2Mo_2O_9$.

As shown in Fig. 2, the PMMA microspheres begin to decompose from 275 °C and they are completely calcined above 385 °C. The infiltrated samples show different decomposition steps. A small weight loss is observed below 50 °C corresponding to removal of residual water. Before starting the degradation of the polymer template a weight change is observed, which is ascribed to dehydration and a first decomposition step of the gel, possibly due to removal of NO_x and carbon species. This is easier to observe in the inset of Fig. 2, where the weight loss for the gel of $La_2Mo_2O_9$ occurs mainly below 300 °C, as suggested by two exothermic peaks observed at 225 and 300 °C, i.e. before the combustion of the PMMA microspheres. This result indicates that solidification and partial decomposition of the citrate gels occur before the PMMA template degradation; hence this method is suitable to obtain macroporous materials. The complete decomposition of the infiltrated samples occurs between 450 and 700 °C as a small weight loss observed at higher temperatures indicates, which may be ascribed to the elimination of residual carbon species. The decomposition temperatures of the different macroporous materials are summarised in Table 1.

The XRD patterns corresponding to the crystalline products are shown in Fig. 3. All the investigated materials are well crystallised after calcination above the decomposition temperature (Table 1) and the targeted fluorite (Fig. 3(a)), perovskite (Fig. 3(b)) and $La_2Mo_2O_9$ structures (not shown) are single phases. The XRD patterns were studied by Rietveld refinement in the corresponding space groups summarised in Table 1. The unit cell parameters and volume cells obtained are consistent with those reported in the ICSD and PDF databases (Table 1).

The average crystallite size diameter was calculated using the Scherrer's equation. The lower crystallite size was obtained for CGO samples with an average diameter of 9 nm, whilst the remaining fluorite and perovskite compounds present slightly larger crystallite sizes (i.e. 12–22 nm) due to the higher calcination temperature required. The larger crystallite size for LMO, approximately 60 nm, is associated to their high degree of sinterability even at rather low temperatures [31].

The microstructure corresponding to the macroporous ionic conductor materials is shown in Fig. 4. A cross-section and surface view respectively of YSZ sample (Fig. 4(a) and (b)), reveals a homogeneous and ordered pore arrangement with uniform thickness of 5–20 μm. LMO and CGO also show a very regular pore distribution as can be observed in Fig. 4(c) and (d). The wall thickness between pores 65 and 90 nm is generally higher than those obtained by infiltration in a previously ordered template, yielding stronger walls that avoid the microstructure collapse, even at relatively high temperatures. The pore sizes estimated from the SEM images were 175–225 nm, which correspond to a 50% of shrinkage compared to the initial microsphere diameter.

TEM images of YSZ (Fig. 5(a)) also reveal a macroporous material with ordered pore arrangement. The walls between pores are formed by aggregates of nanometric particles with a thickness of 25–50 nm (Fig. 5(b)). High resolution TEM images show that the average crystallite size is approximately 10 nm (Fig. 5(c)), similar to those estimated from XRD data. In addition to this, the interplanar distances between atomic columns are consistent with those reported in the literature for YSZ.

The specific surface areas determined by nitrogen sorption range from 11.6 to 38.2 m^2/g, which is in agreement with several other macroporous oxides [18–22]. The lowest specific surface area corresponds to the LMO sample with the largest crystallite size ~60 nm, whereas the largest surface area corresponds to CGO ~38.2 m^2/g with the smallest crystallites, i.e. ~9 nm. These results suggest that samples with lower crystallite sizes exhibit higher specific surface areas.

In addition, YSZ samples were calcined at higher temperatures to investigate the variation of the specific surface area as a function of firing temperature. YSZ samples calcined at 650 °C exhibit a specific surface area of

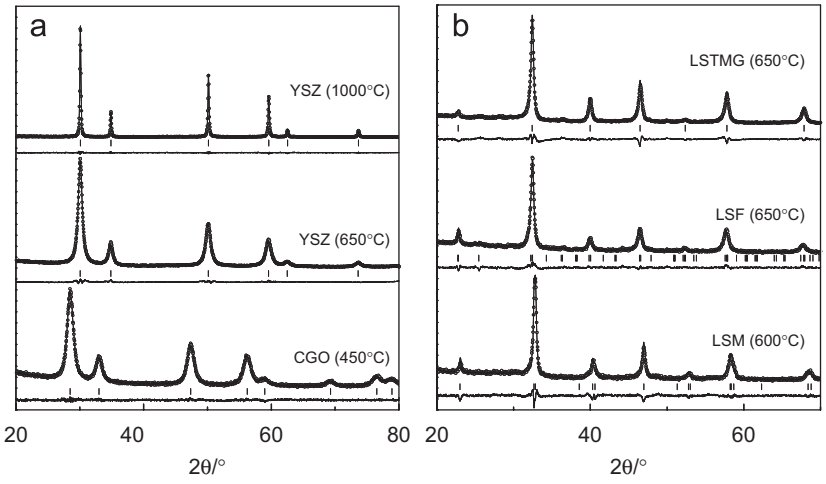

Fig. 3. Rietveld refinement of the macroporous materials with fluorite (a) and perovskite-type structures (b).

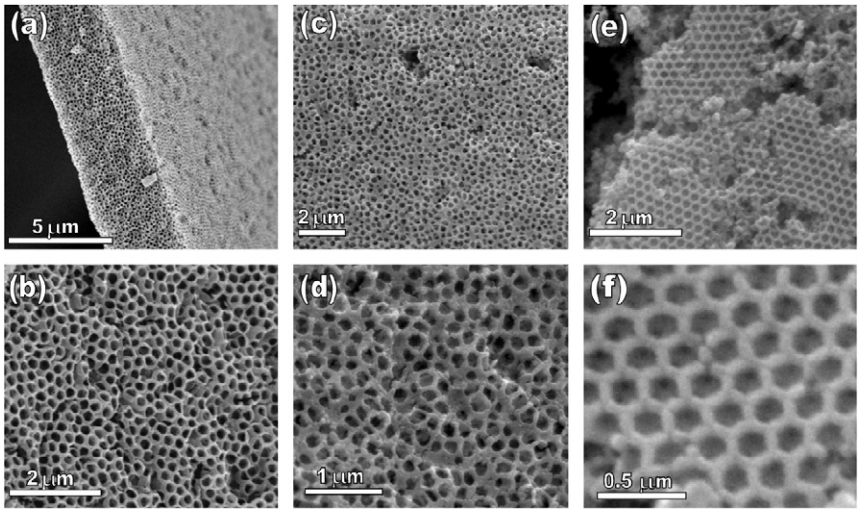

Fig. 4. SEM images of the different electrolytes: (a) and (b) cross-section and surface view, respectively of the YSZ layers; (c) and (d) surface of LMO at different magnifications; (e) and (f) surface of CGO at different magnifications.

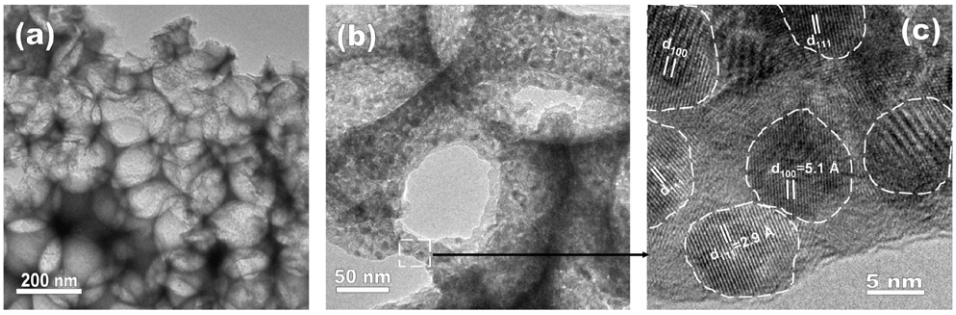

Fig. 5. HRTEM images showing the macroporous microstructure of YSZ (a) formed by nanometric particles (b) of approximately 5–10 nm (c).

21.1 m^2/g, which is slightly reduced from 19.3 to 14.3 m^2/g after firing at 800 and 1000 °C, respectively, for 10 h. In this temperature range, the macroporous microstructure does not collapse and the homogeneous pore distribution is preserved. Consequently, the decrease in BET surface area with increasing of firing temperature is associated to the crystal size growth as can be observed in the diffraction peak broadening of Fig. 3(a). Therefore, these materials present relatively high specific surface even at relatively high firing temperatures, being of interest for SOFCs applications in the low and intermediate temperature range.

Mercury porosimetry measurements further confirmed that the samples exhibit a very homogeneous distribution of pores with porosity of ~48–52% and the estimated average pore sizes agree with those determined by SEM images (Table 2).

Representative images of the synthesised electrodes (i.e. LSM, LSTGM and LSF) are shown in Fig. 6. These materials present high porosity of ~50% with similar crystallite size ~20 nm and specific surface areas between 23 and 27 m^2/g (Tables 1 and 2). It should be noted that the BET surface areas obtained for these materials are similar to those reported in the literature for similar compositions.

Table 2
Microstructural parameters obtained for the macroporous materials

Compound	BET (m^2/g)	ϕ_p (nm)	e (nm)	Porosity (%)	ϕ_p^{Hg} (nm)
CGO	38.3	175	65	48.3	221
YSZ	21.1	205	50	48.2	224
LSF	25.0	200	50	50.6	188
LSM	25.1	220	75	–	–
LSTMG	27.2	200	75	–	–
LMO	11.6	225	90	52.5	228
30%NiO–YSZ	18.7	225	60	55.7	210

Note: ϕ_p: pore size estimate by SEM images; e: wall thickness between pores; and ϕ_p^{Hg}: average pore size evaluated by mercury porosimetry.

For example, Chi et al. [32] reported a value of 24.2 m^2/g for $(La,Ca)MnO_{3-\delta}$ after firing at 800 °C. In comparison, LSM sample prepared in the present work exhibits a specific surface area of 23.4 m^2/g after firing at the same temperature.

The standard anode generally used in SOFC, NiO–YSZ composite, was prepared following the same procedure, using two different concentrations, 30 and 50 wt% of NiO. XRD patterns (Fig. 7) indicate that the fluorite YSZ and

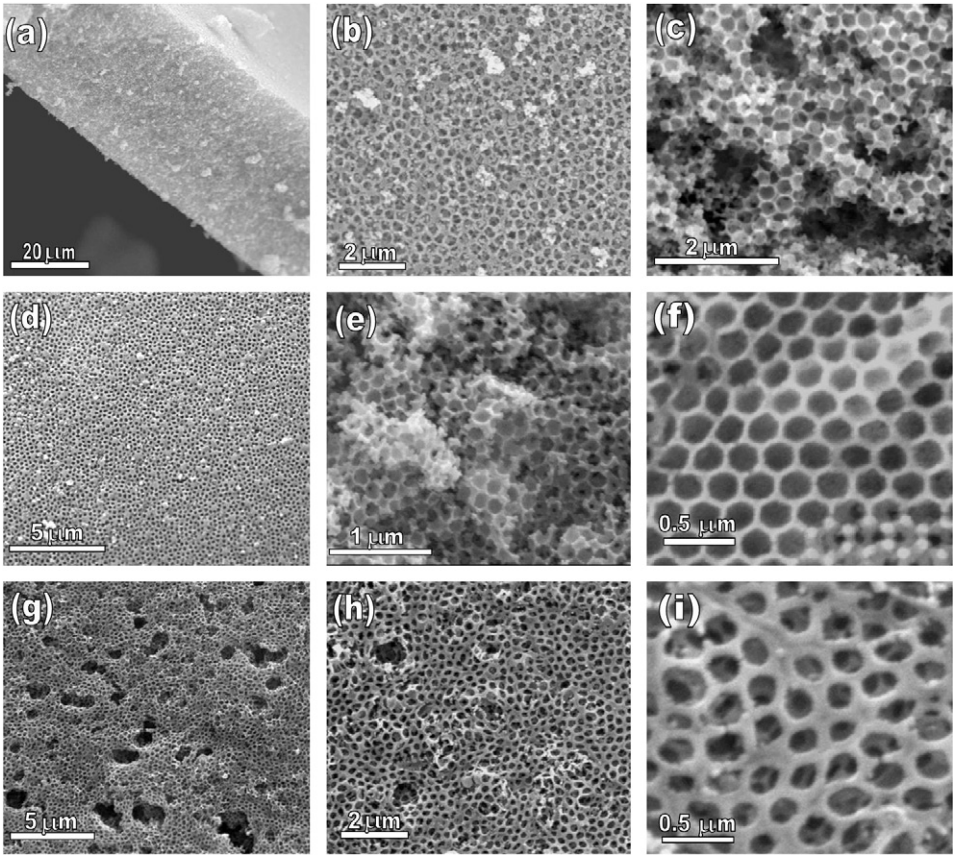

Fig. 6. SEM images revealing the microstructural details of the surface and cross-section view of different electrodes: (a–c) LSM, (d–f) LSF and (g–i) LSTMG.

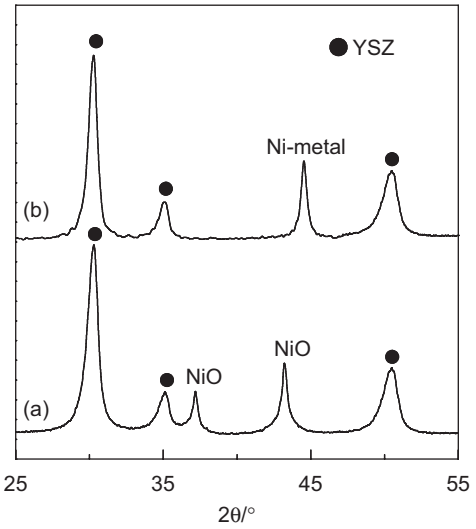

Fig. 7. XRD patterns of the macroporous NiO–YSZ composites prepared in air atmosphere (a) and after reduction under 5%H_2–Ar at 700 °C (b).

NiO structures are obtained after calcination at 650 °C for 5 h. The microstructure reveals an excellent distribution of pores (Fig. 8(a) and (b)), similar to the single-phase samples described above. The TEM images show that the materials are formed by particle aggregates (Fig. 8(d)) and the EDX analysis confirmed that NiO and YSZ particles are uniformly distributed. TEM images at higher magnification show particles for both NiO and YSZ with a diameter of 5–10 nm (Fig. 8(e)). It should be noted that a uniform distribution of YSZ and NiO nanoparticles is very useful as the triple phase boundary region (TPB) is increased. The TPB is defined as the interface where the electronically conductive Ni meets both the YSZ electrolyte and the gaseous species. It is well known that the transport mass and charge transfer processes at the TPB control the efficiency of SOFC anodes. These macroporous materials with uniform porosity facilitate gas diffusion through the pores and its nanocrystalline nature helps to extend the TPB region. Therefore, an enhancement of the performance is expected using this approach in comparison to traditional methods to prepare NiO–YSZ composites. The YSZ–NiO composites were reduced by annealing in 5%H_2–Ar flow at 700 °C for 5 h. The corresponding XRD patterns confirmed that NiO is fully reduced to Ni-metal as shown in Fig. 7. The microstructure for the sample containing 30 wt% of NiO demonstrates that no significant microstructural changes occur after reduction at 700 °C (Fig. 8(c)). However, the macroporous microstructure collapses in the sample with higher NiO content, revealing zones with large particle aggregates and poor porosity after reduction. This is associated to volume change of NiO

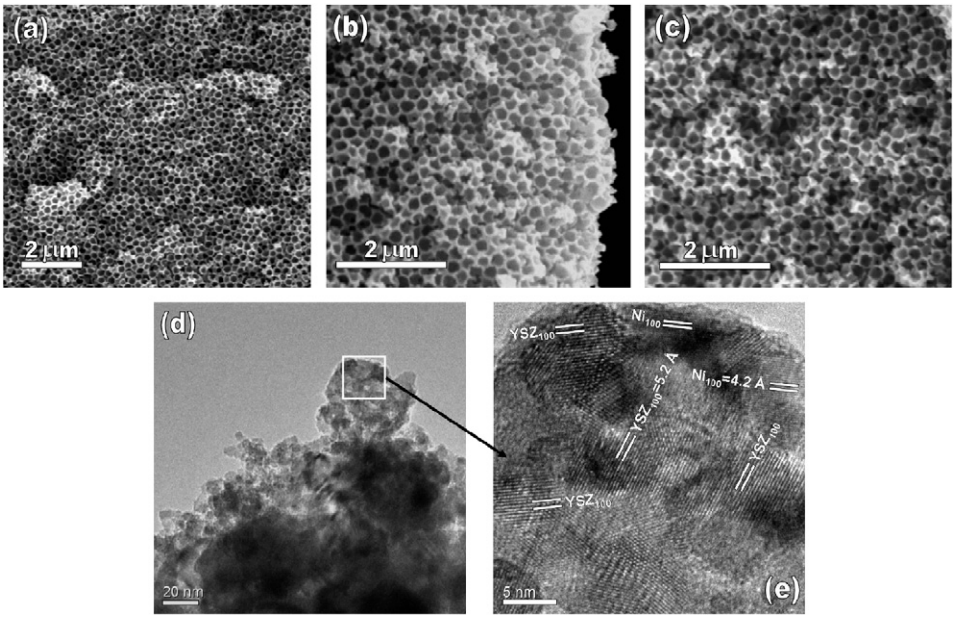

Fig. 8. SEM images of 30 wt% NiO–YSZ composites prepared under air atmosphere at different magnification (a) and (b), and after reduction at 700 °C under 5%H_2–Ar (c). HRTEM images showing the microstructure formed by nanometric (d) and homogenous distribution of NiO and YSZ particles (e).

when reduced to Ni-metal, causing a significant shrinkage of the pores in addition to the agglomeration of nickel particles. Therefore, only materials with low content of NiO $\leqslant$ 30 wt% are stable upon reduction, because YSZ particles are well connected, avoiding an excessive shrinkage of the microstructure. Nevertheless, a 30 wt% of Ni content might be insufficient to create electronic percolation paths and to attain high electronic conductivity. On the other hand, NiO agglomerates at high sintering temperature decreasing the BET surface area from 26.3 m^2/g at 650 °C to 15.6 m^2/g at 800 °C for samples with 50 wt% of NiO. Therefore, the impregnation of the macroporous YSZ material with a Ni-containing solution would be preferable to avoid excessive microstructural changes during reduction.

In summary, the proposed method is useful to prepare thin layer oxides with macroporous structure, with potential application in SOFC devices and catalysis. A similar procedure can be used to deposit thin film of macroporous electrodes on a dense electrolyte. The thickness of the electrodes can be modulated by controlling the solution concentration or depositing several layers. Moreover, the porosity could be modified using polymer spheres with different diameters. In other words, larger PMMA microspheres would give rise to materials with higher porosity, although evidently the mechanical strength would be poorer as the pore size increases. Further work is in progress to deposit thin films of these macroporous electrodes on dense electrolytes and to carry out fuel tests studies. One should note that an improvement of the performance using macroporous/micropores and/or nanocrystalline electrodes has been demonstrated in several reports [16,17,24,33].

4. Conclusions

Oxides materials generally used in SOFCs and catalytic applications, such as ceria and zirconia fluorite-type, manganites, ferrites and titanates perovskite-type structures, have been prepared as thin films using PMMA microspheres as pore former. All investigated materials exhibit homogenous pore distribution with relatively high specific surface area, i.e. between 11 and 38 m^2/g after calcination between 450 and 650 °C. These film materials are interesting for SOFCs application, rendering possibly better performance than usual electrodes made of polycrystalline materials.

Acknowledgments

This work was supported by the Spanish Research program (MAT2004-3856). The authors wish to thank ''Gobierno de Canarias'' for a grant of ''Programa de Incorporación de doctores y tecnólogos a empresas privadas y otras entidades'', (D. M-L) and ''Ministerio de Educación y Ciencia'' for a ''Ramón y Cajal'' fellowship (J.C. R-M and J. C-V). We are also grateful to Luis Hernández (Department of Inorganic Chemistry, University of La Laguna) for technical assistance.

References

[1] N.Q. Minh, T. Takahashi, Science and Technology of Ceramic Fuel Cell, Elsevier, NY, 1995.
[2] B.C.H. Steele, A. Heinzel, Nature 414 (2001) 345.
[3] R.M. Ormerod, Chem. Soc. Rev. 32 (2003) 17.
[4] J. Will, A. Mitterdorfer, C. Kleinlogel, D. Perednis, L.J. Gauckler, Solid State Ionics 131 (2000) 79.

[5] M. Goedickemeier, L.J. Gauckler, J. Electrochem. Soc. 145 (1998) 414.
[6] M. Mogensen, N.M. Sammes, G.A. Tompsett, Solid State Ionics 129 (2000) 63.
[7] T. Ishihara, H. Matsuda, Y. Takita, J. Am. Chem. Soc. 116 (1994) 3801.
[8] P. Lacorre, F. Goutenoire, O. Bohnke, R. Retoux, Y. Laligant, Nature 404 (2000) 856.
[9] V.V. Kharton, F.M.B. Marques, A. Atkinson, Solid State Ionics 174 (2004) 135.
[10] A. Atkinson, S. Barnett, R.J. Gorte, J.T.S. Irvine, A.J. McEvoy, M. Mogensen, S.C. Singhal, J. Vohs, Nat. Mater. 3 (2004) 17.
[11] J.C. Ruiz-Morales, J. Canales-Vázquez, C. Savaniu, D. Marrero-López, W. Zhou, J.T.S. Irvine, Nature 439 (2006) 568.
[12] S.W. Tao, J.T.S. Irvine, Nat. Mater. 2 (2003) 320.
[13] Y.H. Huang, R.I. Dass, Z.L. Xing, J.B. Goodenough, Science 312 (2006) 254.
[14] A.S. Joshi, K.N. Grew, A.A. Peracchio, W.K.S. Chiu, J. Power Sources 164 (2007) 631.
[15] R.M.C. Clemmer, S.F. Corbin, Solid State Ionics 166 (2004) 251.
[16] J.C. Ruiz-Morales, J. Canales-Vázquez, J. Peña-Martínez, D. Marrero-López, J.T.S. Irvine, P. Núñez, J. Mater. Chem. 16 (2006) 540.
[17] Y.L. Zhang, S.W. Zha, M.L. Liu, Adv. Mater. 17 (2005) 487.
[18] R.C. Schroden, A. Stein, in: F. Caruso (Ed.), 3D Ordered Macroporous Material, Colloids and Colloid Assemblies, Willey-VCH Verlag KgaA, Weinhein, Germany, 2004, pp. 465–493.
[19] A. Stein, Microporous Mesoporous Mater. 44 (2001) 227.
[20] M.C. Carbajo, A. Gomez, M.J. Torralvo, E. Enciso, J. Mater. Chem. 12 (2002) 2740.
[21] H. Yan, C. Christopher, F. Blandford, B.T. Holland, W.H. Smyrl, A. Stein, Chem. Mater. 12 (2000) 1134.
[22] M. Sadakane, T. Asanuma, J. Kubo, W. Ueda, Chem. Mater. 17 (2005) 3546.
[23] M. Boaro, J.M. Vohs, R.J. Gorte, J. Am. Ceram. Soc. 86 (2003) 395.
[24] M. Mamak, N. Coombs, G.A. Ozin, Chem. Commun. 20 (2002) 2300.
[25] M. Mamak, N. Coombs, G.A. Ozin, J. Am. Chem. Soc. 122 (2000) 8932.
[26] Y.-H. Koh, J.-J. Sun, H.-E. Kim, Mater. Lett. 61 (2007) 1283.
[27] I.M. Hung, H.P. Wang, W.H. Lai, K.Z. Fung, M.H. Hon, Electrochim. Acta 50 (2004) 745.
[28] D. Zou, J.J. Aklonis, R. Salovey, J. Polym. Sci. Part A: Polym. Chem. 30 (1992) 2443.
[29] J. Rodríguez-Carvajal, Phys. B: Condens. Matter 192 (1993) 55.
[30] T. Roisnel, J. Rodríguez-Carvajal, WinPLOTR, Laboratoire Léon Brillouin-LCSI, France, 2005.
[31] D. Marrero-López, J. Peña-Martínez, D. Pérez-Coll, P. Núñez, J. Alloys Compd. 422 (2006) 249.
[32] E.O. Chi, Y.N. Kim, J.C. Kim, N.H. Hur, Chem. Mater. 15 (2003) 1929.
[33] J.M. Serra, S. Uhlenbruck, W.A. Meulenberg, H.P. Buchkremer, D. Stöver, Top. Catal. 40 (2006) 123.